Higher-order topological phases in a spring-mass model on a breathing kagome lattice

Hiromasa Wakao,[1,*] Tsuneya Yoshida,[2] Hiromu Araki,[1] Tomonari Mizoguchi,[2] and Yasuhiro Hatsugai[2]
[1]*Graduate School of Pure and Applied Sciences, University of Tsukuba, Tsukuba, Ibaraki 305-8571, Japan*
[2]*Department of Physics, University of Tsukuba, Tsukuba, Ibaraki 305-8571, Japan*

(Received 18 September 2019; accepted 6 March 2020; published 30 March 2020)

We propose a realization of higher-order topological phases in a spring-mass model with a breathing kagome structure. To demonstrate the existence of the higher-order topological phases, we characterize the topological properties and show that the corner states appear under the fixed boundary condition. To characterize the topological properties, we introduce a formula for the $\mathbb{Z}_3$ Berry phases in the Brillouin zone. From the numerical result of this $\mathbb{Z}_3$ Berry phase, we have elucidated that coupling between the longitudinal and transverse modes yields a state characterized by the Berry phase $\frac{2\pi}{3}$ for our mechanical breathing kagome model. In addition, we suggest that the corner states can be detected experimentally through a forced vibration.

DOI: 10.1103/PhysRevB.101.094107

I. INTRODUCTION

Topological insulators (TIs) [1,2] are a distinctive class of insulators where topologically nontrivial structures of Bloch wave functions give rise to characteristic boundary states. Various unique phenomena are caused by these boundary states, such as quantization of Hall [3] and spin-Hall conductivities [4] and electromagnetic responses [5,6]. In TIs, bulk topological invariants which characterize the nontrivial topology of Bloch wave functions are known to be related to the $(d-1)$-dimensional boundary states (with d being the spatial dimension of the bulk Hamiltonian); this relation is nowadays established as bulk-boundary correspondence [7,8].

Recently, a novel class of TIs, called higher-order topological insulators (HOTIs), was introduced [9–16]. In HOTIs, $d-2$ or fewer dimensional boundary states appear in d-dimensional models, which is predicted by topological invariants in the bulk. Examples of such topological invariants include the multipole moment [10,17], the nested Wilson loops [11,15], the quantized Wannier centers [12], the entanglement polarization [18], and the $\mathbb{Z}_Q$ Berry phase [19–21]. In that sense, a novel kind of bulk-boundary correspondence emerges in HOTIs.

In parallel with the theoretical developments, realization of HOTIs in solids has actively been pursued [22–27]. In addition, higher-order topological phases in artificial systems have also been studied intensively. These systems are advantageous compared with solids from the viewpoints of simplicity of experimental setup and high tunability of parameters, which enable us to implement desirable structures to realize higher-order topological phases. Indeed, the higher-order topological phases were realized in mechanical systems [28,29], photonic crystals [30,31], phononic crystals [32–34], electrical circuits [35,36], and carbon monoxide molecules on a Cu(111) surface [37].

In this paper, we propose a realization of higher-order topological phases in a spring-mass model. Spring-mass models, composed of a periodic alignment of springs and mass points, serve as a simple platform to realize topological phenomena governed by Newton's equation of motion [38–43]. Indeed, topological phases accompanied by characteristic boundary states, such as Chern insulators [39,40], nodal-line semimetals [41], and Weyl semimetals [42], were proposed. These results motivated us to study the higher-order topological phase in a spring-mass model.

As a concrete example, we study the spring-mass model on a breathing kagome lattice and demonstrate the realization of the higher-order topological phase in our model. Specifically, we characterize the topological phases by introducing a formula for the $\mathbb{Z}_3$ Berry phase in the Brillouin zone and the existence of the corner states. In addition, from this numerical result for these bulk properties, we have elucidated that coupling between the longitudinal and the transverse modes yields a state characterized by the Berry phase $\frac{2\pi}{3}$ for our mechanical breathing kagome model. We further propose how to observe the corner states experimentally. To this aim, we study the dynamics under the external force and show the characteristic behavior of corner states distinct from the bulk states.

The rest of this paper is organized as follows. In Sec. II, we introduce the spring-mass model on a breathing kagome lattice and explain how to describe the motion of mass points in this model. In Sec. III, we first explain the definition of the $\mathbb{Z}_3$ Berry phases in momentum space. We then show the numerical results for the bulk properties such as band structures and $\mathbb{Z}_3$ Berry phases. In Sec. IV, we elucidate the existence of the corner states in this model under the fixed boundary conditions with a triangle arrangement. In Sec. V, we demonstrate that the corner states can be observed by the forced vibration. In Sec. VI, we present a summary of this paper. In Appendix A, we see the $\mathbb{Z}_3$ Berry phase for the lower five bands, which accounts for the corner states under the weak tension. In Appendix B, we show the band structure on the cylinder geometry. In Appendix C, we show

*wakao@rhodia.ph.tsukuba.ac.jp

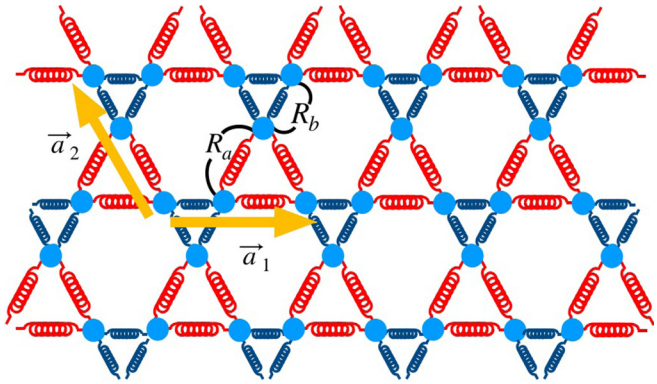

FIG. 1. A spring-mass model in a breathing kagome structure.

the numerical result of the inverse participation ratio (IPR) to see the corner states from the bulk or edge continuum. In Appendix D, we show the existence of the corner state under the fixed boundary conditions within a parallelogram arrangement.

II. A SPRING-MASS MODEL ON A BREATHING KAGOME LATTICE

We consider a system consists of the mass points aligned on a breathing kagome lattice and springs connecting the masses (Fig. 1). The spring constants of red springs on upward triangles are t_a, and those of blue springs on downward triangles are t_b. We label a red spring (a blue spring) as $\alpha = a$ (b). Henceforth, we set the mass as unity for simplicity.

We set unit vectors $\vec{a}_1$ and $\vec{a}_2$ as

$$\vec{a}_1 = (R_a + R_b)\begin{pmatrix} 1 \\ 0 \end{pmatrix} \tag{1a}$$

and

$$\vec{a}_2 = (R_a + R_b)\begin{pmatrix} -\frac{1}{2} \\ \frac{\sqrt{3}}{2} \end{pmatrix}, \tag{1b}$$

where R_a and R_b denote lengths of red springs and blue springs in equilibrium, respectively. To make the model be in equilibrium, we have to take into account a balances of forces, which is satisfied for

$$t_a(R_a - l_a) = t_b(R_b - l_b), \tag{2}$$

where l_α is the natural length of a spring. In the following, we set $l_a = l_b = 1$.

Let us see how to describe the motion of mass points. Dynamical variables are $\vec{x}_{\vec{R},p}$, which are displacements of the mass points from the position in equilibrium. Here, a pair of indices $\vec{R}$ and p specifies the lattice points; $\vec{R}$ denotes the position of the unit cell, and $p = 1, 2, 3$ denotes a sublattice. For later use, we introduce $\vec{r}_p$, which denotes the position of sublattice p within the unit cell. The Lagrangian describing the motion of masses is written as [40]

$$\mathcal{L} = \frac{1}{2}\sum_{\vec{R}}\sum_{p}\left(\dot{x}^{\mu}_{\vec{R},p}\right)^2 - \frac{1}{2}\sum_{\langle \vec{R},p;\vec{R}',q\rangle}\left(x^{\mu}_{\vec{R},p} - x^{\mu}_{\vec{R}',q}\right) \times \gamma^{\mu\nu}_{\vec{R}+\vec{r}_p-\vec{R}'-\vec{r}_q}\left(x^{\nu}_{\vec{R},p} - x^{\nu}_{\vec{R}',q}\right), \tag{3}$$

where $\langle \vec{R}, p; \vec{R}', q\rangle$ means nearest-neighbor pairs of the mass points, $\mu, \nu = x, y$ are directions in a two-dimensional space, and the explicit form of $\gamma^{\mu\nu}_{\vec{R}+\vec{r}_p-\vec{R}'-\vec{r}_q}$ is $\gamma^{\mu\nu}_{\vec{R}+\vec{r}_p-\vec{R}'-\vec{r}_q} = t_\alpha\{(1-\eta_\alpha)\delta_{\mu\nu} + \eta_\alpha \hat{X}^\mu \hat{X}^\nu\}$. Here, $\vec{X} = \vec{R} + \vec{r}_p - \vec{R}' - \vec{r}_q$, and $\hat{X}^\mu = X^\mu/|\vec{X}|$. The parameter η_α is defined as

$$\eta_\alpha = \frac{l_\alpha}{R_\alpha}, \tag{4}$$

which denotes the strength of tensions of springs. Notice that the index α in $\gamma^{\mu\nu}_{\vec{R}+\vec{r}_p-\vec{R}'-\vec{r}_q}$ is naturally determined once we specify the nearest-neighbor pair $\langle \vec{R}, p; \vec{R}', q\rangle$. The first term in Eq. (3) is the kinetic energy, while the second term is the potential energy of the springs.

Then, the Euler-Lagrange equation for $x^{\mu}_{\vec{R},p}$,

$$\frac{d}{dt}\left(\frac{\partial \mathcal{L}}{\partial \dot{x}^{\mu}_{\vec{R},p}}\right) - \frac{\partial \mathcal{L}}{\partial x^{\mu}_{\vec{R},p}} = 0, \tag{5}$$

can be written as a coupled differential equation,

$$\ddot{\vec{x}} + D\vec{x} = 0, \tag{6}$$

where $\vec{x}$ is the column vector obtained by aligned $x^{\mu}_{\vec{R},p}$. The matrix D,

$$(D)_{\vec{R},p,\mu;\vec{R}',q,\nu} = \left(\sum_{\langle \vec{R},p;\vec{R}''o\rangle}\gamma^{\mu\nu}_{\vec{R}+\vec{r}_p-\vec{R}''-\vec{r}_o}\right)\delta_{\vec{R},\vec{R}'}\delta_{p,q} - \gamma^{\mu\nu}_{\vec{R}+\vec{r}_p-\vec{R}'-\vec{r}_q}, \tag{7}$$

is a real-space dynamical matrix. Assuming the mass points oscillate with a frequency ω, we can write $x^{\mu}_{\vec{R},p} = e^{i\omega t}\xi^{\mu}_{\vec{R},p}$. Substituting this into Eq. (6), we obtain

$$-\omega^2\vec{\xi} + D\vec{\xi} = 0. \tag{8}$$

Equation (8) is an eigenvalue equation of the matrix D whose basis is $\xi^{\mu}_{\vec{R},p}$ and eigenvalue is ω^2. This equation describes the motion of masses in a spring-mass model in real space.

Under the periodic boundary condition, the translational invariance of the system results in the eigenvalue equation in the momentum space. First, we apply the Fourier transformation

$$x^{\mu}_{\vec{R},p} = \frac{1}{N}\sum_{\vec{k}} e^{i\vec{k}\cdot\vec{R}}u^{\mu}_{\vec{k},p}. \tag{9}$$

Substituting Eq. (9) into Eq. (3), the Lagrangian is written as

$$\mathcal{L} = \frac{1}{N}\sum_{\vec{k}}\left\{\frac{1}{2}\sum_{p}\dot{u}^{\mu}_{\vec{k},p}\dot{u}^{\mu}_{-\vec{k},p} - \frac{1}{2}\sum_{pq}\Gamma^{\mu\nu}_{pq}(\vec{k})u^{\mu}_{\vec{k},p}u^{\nu}_{-\vec{k},q}\right\}, \tag{10a}$$

with

$$\Gamma^{\mu\nu}_{pq}(\vec{k}) = \sum_{\vec{R}}(D)_{\vec{0},p,\mu;\vec{R},q,\nu}e^{i\vec{k}\cdot\vec{R}}. \tag{10b}$$

The matrix Γ is called a momentum-space dynamical matrix. The dimension of the momentum-space dynamical matrix in this model is six since there are three

sublattices and two spatial coordinates. Under the basis $(u^x_{\vec{k},1}, u^y_{\vec{k},1}, u^x_{\vec{k},2}, u^y_{\vec{k},2}, u^x_{\vec{k},3}, u^y_{\vec{k},3})^{\mathrm{T}}$, the explicit form of $\Gamma(\vec{k})$ is

$$\Gamma = \begin{pmatrix} D_1 & -\gamma_{12}(\vec{k}) & -\gamma_{13}(\vec{k}) \\ -\gamma^\dagger_{12}(\vec{k}) & D_2 & -\gamma_{23}(\vec{k}) \\ -\gamma^\dagger_{13}(\vec{k}) & -\gamma^\dagger_{23}(\vec{k}) & D_3 \end{pmatrix}, \tag{11a}$$

with

$$\gamma_{12}(\vec{k}) = \gamma_{12a} + e^{-i(\vec{a}_1+\vec{a}_2)\cdot\vec{k}}\gamma_{12b}, \tag{11b}$$

$$\gamma_{13}(\vec{k}) = \gamma_{13a} + e^{-i\vec{a}_1\cdot\vec{k}}\gamma_{13b}, \tag{11c}$$

$$\gamma_{23}(\vec{k}) = \gamma_{23a} + e^{-i\vec{a}_2\cdot\vec{k}}\gamma_{23b} \tag{11d}$$

and

$$D_1 = \gamma_{12a} + \gamma_{13a} + \gamma_{12b} + \gamma_{13b}, \tag{11e}$$

$$D_2 = \gamma_{12a} + \gamma_{23a} + \gamma_{12b} + \gamma_{23b}, \tag{11f}$$

$$D_3 = \gamma_{23a} + \gamma_{13a} + \gamma_{23b} + \gamma_{13b}. \tag{11g}$$

Here, $\gamma_{12\alpha}$, $\gamma_{13\alpha}$, and $\gamma_{23\alpha}$ are defined as

$$\gamma_{12\alpha} = t_\alpha \left\{ (1-\eta_\alpha)\begin{pmatrix} 1 & 0 \\ 0 & 1 \end{pmatrix} + \eta_\alpha \begin{pmatrix} \frac{1}{4} & \frac{\sqrt{3}}{4} \\ \frac{\sqrt{3}}{4} & \frac{3}{4} \end{pmatrix} \right\}, \tag{11h}$$

$$\gamma_{13\alpha} = t_\alpha \left\{ (1-\eta_\alpha)\begin{pmatrix} 1 & 0 \\ 0 & 1 \end{pmatrix} + \eta_\alpha \begin{pmatrix} 1 & 0 \\ 0 & 0 \end{pmatrix} \right\}, \tag{11i}$$

$$\gamma_{23\alpha} = t_\alpha \left\{ (1-\eta_\alpha)\begin{pmatrix} 1 & 0 \\ 0 & 1 \end{pmatrix} + \eta_\alpha \begin{pmatrix} \frac{1}{4} & -\frac{\sqrt{3}}{4} \\ -\frac{\sqrt{3}}{4} & \frac{3}{4} \end{pmatrix} \right\}. \tag{11j}$$

The Euler-Lagrange equation for $u^\mu_{\vec{k},p}$ is written as

$$\frac{d}{dt}\left(\frac{\partial \mathcal{L}}{\partial \dot{u}^\mu_{\vec{k},p}}\right) - \frac{\partial \mathcal{L}}{\partial u^\mu_{\vec{k},p}} = 0. \tag{12}$$

This leads to an equation of motion under the periodic boundary condition,

$$\ddot{u}^\mu_{\vec{k},p} + \sum_q \Gamma^{\mu\nu}_{pq}(\vec{k}) u^\mu_{\vec{k},p} = 0. \tag{13}$$

Writing the time independence of $u^\mu_{\vec{k},p}$ as

$$u^\mu_{\vec{k},p} = e^{-i\omega t}\phi^\mu_p(\vec{k}), \tag{14}$$

we obtain the Euler-Lagrange equation reduced to the eigenvalue equation

$$-\omega^2\phi^\mu_p(\vec{k}) + \sum_q \Gamma^{\mu\nu}_{pq}(\vec{k})\phi^\nu_q(\vec{k}) = 0. \tag{15}$$

By solving the eigenvalue equation (15), we obtain the dispersion relation, which we will discuss in the next section.

Before closing this section, we address the correspondence between the spring-mass model and the tight-binding model. In fact, the spring-mass model is reduced to two copies of the tight-binding model if we set $\eta_a = 0$, $\eta_b = 0$, i.e., the tension is infinitely strong [44], since the off-diagonal parts of the matrix $\gamma_{ij\alpha}$ vanish [see Eqs. (11h)–(11j)].

III. $\mathbb{Z}_3$ BERRY PHASE

A. $\mathbb{Z}_3$ Berry phase in momentum space

In this section, we introduce the $\mathbb{Z}_3$ Berry phase defined in momentum space. The key idea originates from the quantized Berry phase with respect to the local twists of the Hamiltonian [19–21,45–54]. Such a Berry phase has been used as a topological order parameter for various topological phases, especially in correlated systems such as spin systems [45–53]. The Berry phase is quantized due to symmetries, e.g., time-reversal symmetry, inversion symmetry, and discrete rotational symmetry. Recently, it was also used to characterize the HOTI phases [20,21,54].

Here, we show that such a Berry phase can also be defined in the momentum-space representation for the breathing-kagome-lattice spring-mass model. Extension of the $\mathbb{Z}_3$ Berry phase in momentum space is important from the viewpoint of computational costs. Namely, to calculate the quantized Berry phase with respect to the local twists of the Hamiltonian, one has to calculate the many-body ground state under the local twist. On the other hand, the single-particle eigenfunctions are enough to calculate the $\mathbb{Z}_3$ Berry phase in momentum space; thus, we can save computational costs when dealing with noninteracting quantum systems and classical systems.

The $\mathbb{Z}_3$ Berry phase for the lowest νth bands γ^ν is defined as follows. First, we define the $\nu \times \nu$ Berry connection matrix:

$$\vec{A}^\nu(\vec{k}) = i\Phi^{\nu\dagger}(\vec{k})\frac{\partial}{\partial \vec{k}}\Phi^\nu(\vec{k}), \tag{16}$$

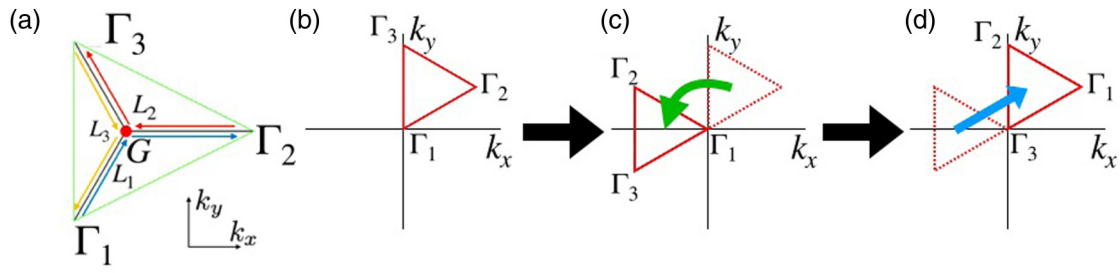

FIG. 2. (a) The paths in momentum space. The coordinates of Γ_1, Γ_2, and Γ_3 are (0,0), $\frac{2\pi}{R_a+R_b}(1, \frac{1}{\sqrt{3}})$, and $\frac{2\pi}{R_a+R_b}(0, \frac{2}{\sqrt{3}})$, respectively. The G point is $\frac{2\pi}{R_a+R_b}(\frac{1}{3}, \frac{1}{\sqrt{3}})$. The path L_i is $\Gamma_i \to G \to \Gamma_{i+1}$ ($\Gamma_4 = \Gamma_1$). (b) The triangle area whose vertices are Γ_1, Γ_2, Γ_3. (c) and (d) Schematic figures for the operations which keep the Hamiltonian invariant. (c) The 120° rotation of the triangle area in momentum space. (d) The translation of the triangle area in momentum space. Combining these two operations, the Γ_i point is transformed to Γ_{i+1} with $\Gamma_4 := \Gamma_1$. Consequently, the path L_i is transformed to L_{i+1} with $L_4 = L_1$.

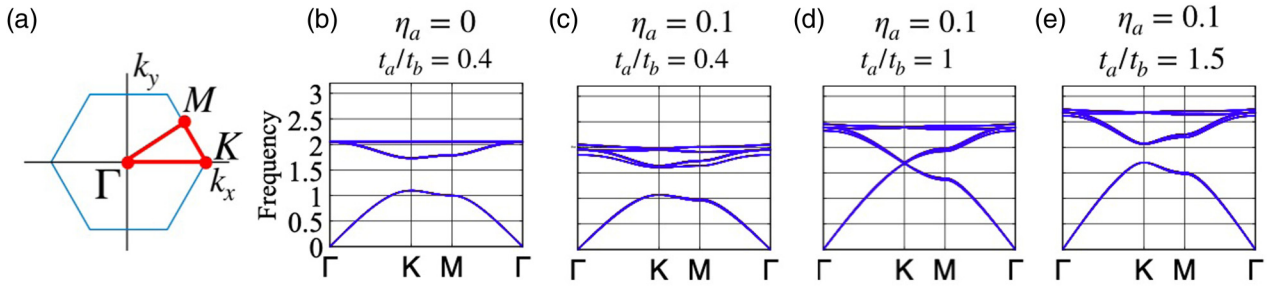

FIG. 3. Bulk properties of the spring-mass model. (a) The first Brillouin zone of the spring-mass model. The Γ, K, and M points are located at $(k_x, k_y) = (0, 0)$, $\frac{2\pi}{R_a+R_b}(\frac{2}{3}, 0)$, and $\frac{2\pi}{R_a+R_b}(\frac{1}{2}, \frac{1}{2\sqrt{3}})$, respectively. (b)–(e) The band structure along the line shown in (a) for several parameter sets $(\eta_\alpha, t_a/t_b)$. (b), (c), (d), and (e) show the data for $(\eta_\alpha, t_a/t_b) = (0, 0.4)$, (0.1,0.4), (0.1,1), and (0.1,1.5), respectively.

where

$$\Phi^\nu(\vec{k}) = [\vec{\phi}_1(\vec{k}), \quad \ldots \quad , \vec{\phi}_\nu(\vec{k})] = \begin{pmatrix} (\phi_1)_1 & (\phi_2)_1 & \cdots & (\phi_\nu)_1 \\ \vdots & \vdots & \ddots & \vdots \\ (\phi_1)_6 & (\phi_2)_6 & \cdots & (\phi_\nu)_6 \end{pmatrix} \tag{17}$$

is the $6 \times \nu$ matrix composed of the eigenvectors of a momentum-space dynamical matrix in the spring-mass model on the breathing kagome lattice, represented by $\vec{\phi}_n(\vec{k})$. Then, the Berry phase for the lowest ν bands is expressed as

$$\gamma^\nu(L_i) = \int_{L_i} \mathrm{Tr}\,[\vec{A}^\nu(\vec{k})] \cdot d\vec{k}, \tag{18}$$

where L_i $(i = 1, 2, 3)$ is a path in momentum space, $L_i : \Gamma_i \to G \to \Gamma_{i+1}(\Gamma_4 = \Gamma_1)$ [Fig. 2(a)].

In the spring-mass model on a breathing kagome lattice, the momentum-space dynamical matrix is invariant under the threefold rotation in momentum space (Fig. 2). We define this operator as U. The momentum-space dynamical matrix has a symmetry which is expressed as

$$U\Gamma(k_i)U^{-1} = \Gamma(C_3 k_i), \tag{19}$$

with $k_i \in L_i$ and L_i being a path in momentum space, $L_i : \Gamma_i \to G \to \Gamma_{i+1}$. Here, we have supposed that the momentum k_i is mapped to $C_3 k_i \in L_{i+1}$ by applying C_3 rotation. This relation indicates that the Berry phases $\gamma^\nu(L_i)$ computed along each path take the same value,

$$\gamma^\nu(L_1) = \gamma^\nu(L_2) = \gamma^\nu(L_3). \tag{20}$$

In addition, the integral along the path $L_1 + L_2 + L_3$ is equal to zero,

$$\sum_{i=1}^{3} \gamma^\nu(L_i) = 0 \mod 2\pi. \tag{21}$$

From Eqs. (20) and (21),

$$\gamma^\nu \equiv \gamma^\nu(L_i) = \frac{2\pi k}{3} \mod 2\pi, \tag{22}$$

where k is 0, 1, or 2. The same argument can be applied to a tight-binding model on a breathing kagome lattice by replacing the momentum-space dynamical matrix Γ with the Hamiltonian H since H preserves threefold rotational symmetry and translational symmetry. Note that, in the spring-mass models, the rotation is applied not only to the momentum and sublattice degrees of freedom but also to directions of the displacement $(\mu = x, y)$.

In fact, the $\mathbb{Z}_3$ Berry phase in momentum space is equivalent to the local-twist Berry phase discussed in Ref. [19]. To see this, we consider the $\mathbb{Z}_3$ Berry phase in momentum space, where the upward triangle is a unit cell. In this case, there is the phase factor from the Bloch wave vector for hoppings from a site in the upward triangle to a site in the downward triangle. By replacing the factors $e^{-i\vec{k}\cdot\vec{a}_1}$ and $e^{-i\vec{k}\cdot\vec{a}_2}$ with the twisting parameters $e^{i\theta_1}$ and $e^{i\theta_2}$ respectively, we find that the $\mathbb{Z}_3$ Berry phase in momentum space is the same as the local-twist Berry phase for the 1×1 unit cell of the downward triangle. A similar correspondence also holds for the Su-Schrieffer-Heeger model [55] and the breathing pyrochlore model.

B. Bulk properties

In this section, we present the properties of this model under the periodic boundary condition. To be specific, we investigate the dispersion relation and the bulk topological invariant. First, we show the band structures obtained by diagonalizing the momentum-space dynamical matrix [Figs. 3(b)–3(e)]. Here, the horizontal axis denotes the high-symmetry lines in the Brillouin zone, with Γ, K, and M denoting the high-symmetry points [Fig. 3(a)].

There are six bands; for $\eta_a = 0$, we see three bands, each of which is doubly degenerate. For $\eta_a \neq 0$, twofold degeneracy is lifted because of the coupling between transverse waves and longitudinal waves [Figs. 3(b) and 3(c)]. Moreover, there are no flat bands unless $\eta_a = 0$. These are the unique characters of the spring-mass model which are different from the tight-binding model.

In Fig. 4(a), we show the numerical results for the $\mathbb{Z}_3$ Berry phase with $\nu = 2$. For the numerical calculation, we employ the method introduced in Ref. [56] to avoid the difficulties

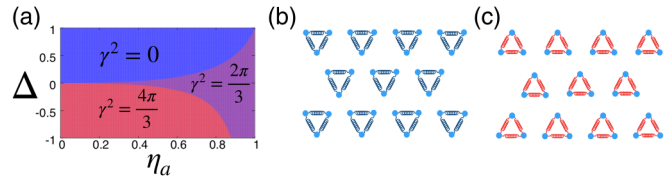

FIG. 4. (a) The Berry phase for the lowest two bands. Schematic figures for two limits with (b) $t_a = 0$ and (c) $t_b = 0$.

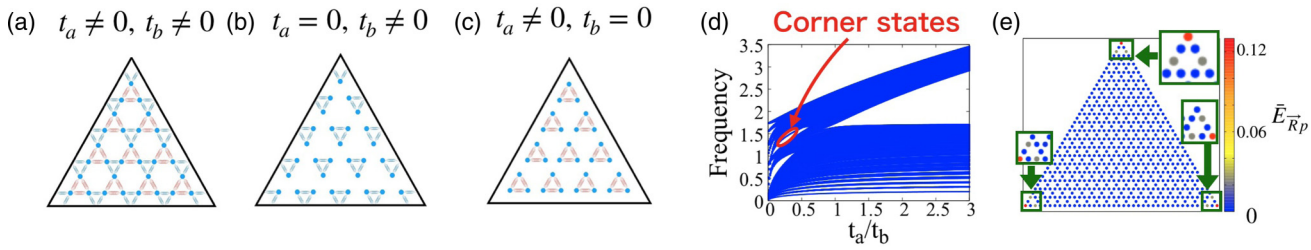

FIG. 5. Schematic figures for the spring-mass model in a triangle arrangement for (a) $t_a \neq 0, t_b \neq 0$, (b) $t_a = 0, t_b \neq 0$, and (c) $t_a \neq 0, t_b = 0$. Black lines represent walls. (d) Eigenfrequencies as a function of t_a/t_b for $\eta_a = 0.1$ with a triangle arrangement. (e) Kinetic-energy distribution in the real space of the corner states for $t_a/t_b = 0.4$. We write the number of small triangles along the edge as L; the total number of masses is $3L(L+1)/2$.

in the gauge choice. Note that the $\mathbb{Z}_3$ Berry phase cannot be defined for $\eta_a = 1$ because the gap between the lowest second and third bands is closed. To map out the $\mathbb{Z}_3$ Berry phase in the parameter space, we introduce $\Delta \in [-1, 1]$, describing the degrees of breathing. More precisely, Δ relates t_a and t_b as

$$t_a = 1 + \Delta \tag{23a}$$

and

$$t_b = 1 - \Delta. \tag{23b}$$

For $\Delta = 1$ (-1), the system is reduced to a set of isolated triangles of mass points connected by red (blue) springs. We note that $t_b = 0$ $(t_a = 0)$ holds for $\Delta = 1$ (-1). For $\Delta = 0$, the mass points form an isotropic kagome lattice because $t_a = t_b$ holds.

We see in Fig. 4(a) that there are three phases where the $\mathbb{Z}_3$ Berry phase takes $\gamma = 0$, $\frac{2\pi}{3}$, and $\frac{4\pi}{3}$, respectively. Among them, the phase with $\gamma = \frac{2\pi}{3}$ is the new phase which does not have a counterpart in the tight-binding model. In fact, this phase originates from the interaction between the longitudinal and transverse waves inherent in the spring-mass model. We can observe the gap closing between the second and third bands when the $\mathbb{Z}_3$ Berry phase changes [see Figs. 3(c)–3(e)]. In other words, the $\mathbb{Z}_3$ Berry phase is the topological invariant, so its value does not change as long as the band gap is not closed. This indicates that the system can be adiabatically deformed to a certain limit that has the same Berry phase. In the present model, for small η_a, the phase with $\gamma = \frac{4\pi}{3}$ is connected to the limit of $\Delta = -1$ (i.e., $t_a = 0$), while the phase with $\gamma = 0$ is connected to the limit of $\Delta = 1$ (i.e., $t_b = 0$). The schematic figures for the former and the latter are illustrated in Figs. 4(b) and 4(c), respectively. This physical picture of the adiabatic connection to the decoupled triangles is essential to understand the bulk-corner correspondence in this system, as we will explain in the next section.

IV. CORNER STATES UNDER THE FIXED BOUNDARY CONDITION

In this section, we demonstrate that system hosts corner states due to topological properties in the bulk. This bulk-corner correspondence serves as direct evidence of the higher-order topological phase. Specifically, considering a triangle arrangement [12] (Fig. 5), we numerically show that the corner states emerge for $\gamma^2 = 4\pi/3$ while they do not for $\gamma^2 = 0$.

Before going to the numerical results, we consider two limits, i.e., $t_a = 0$ [Fig. 5(b)] and $t_b = 0$ [Fig. 5(c)], to gain insight into the boundary states. Note that, in these limits, the equilibrium condition of Eq. (2) is inevitably broken. Nevertheless, it is helpful to consider these limits, as we explain below. For $t_a = 0,\ t_b \neq 0$ [Fig. 5(b)], there exist three isolated mass points connected only to the wall at three corners of the triangle. This configuration supports the eigenmodes localized at the corners. In contrast to this, there are no isolated mass points for $t_a \neq 0,\ t_b = 0$ [Fig. 5(c)]. From these insights, we expect that three corner states exist for $t_a \ll t_b$, while they do not for $t_b \ll t_a$.

Keeping this observation in mind, let us move on to the numerical results. In Fig. 5(d), we plot the energy spectra as a function of t_a/t_b for $\eta_a = 0.1$ and $L = 20$ (see Appendix A for the result for large η_a). We see the existence of the in-gap states for a certain region of $t_a/t_b < 1$, encircled by a red ellipse in Fig. 5(d). Note that these corner states have quasithreefold degeneracy for $\eta_a \neq 0$. We also note that, even for $t_a/t_b < 1$, the corner states may be energetically buried in the bulk or edge states; thus, they cannot be seen in the energy spectra of Fig. 5(d); for the edge state of the present model, see Appendix B. To avoid this problem, we calculate the IPR and show the corner states in the bulk or edge continuum (see Appendix C). Figure 5(e) indicates that the in-gap states observed above correspond to the corner states. This figure shows the kinetic-energy distribution

$$\bar{E}_{\vec{R},p} = \frac{1}{4N_c} \sum_{\ell=1}^{N_c} \left(\omega_\ell I^\ell_{\vec{R},p}\right)^2 \tag{24}$$

for these quasidegenerate in-gap states. Here, $I^\ell_{\vec{R},p} = \sqrt{(\xi^{\ell,x}_{\vec{R},p})^2 + (\xi^{\ell,y}_{\vec{R},p})^2}$ is the amplitude of the displacement of the mass point $(\vec{R}, p)$ of the mode ℓ. The summation in Eq. (24) is taken over the N_c-fold (quasi)degenerate states. In Fig. 5(e), we can clearly see that the kinetic-energy distribution is localized at the corners, manifesting the existence of the higher-order topological phase in the present model.

Combining the above results and the fact that the $\mathbb{Z}_3$ Berry phase γ^2 takes $4\pi/3$ for $t_a/t_b < 1$ (see Fig. 4), we can confirm that the bulk-corner correspondence holds for our spring-mass model. This is a direct consequence of the adiabatic connection argument we presented in Sec. III.

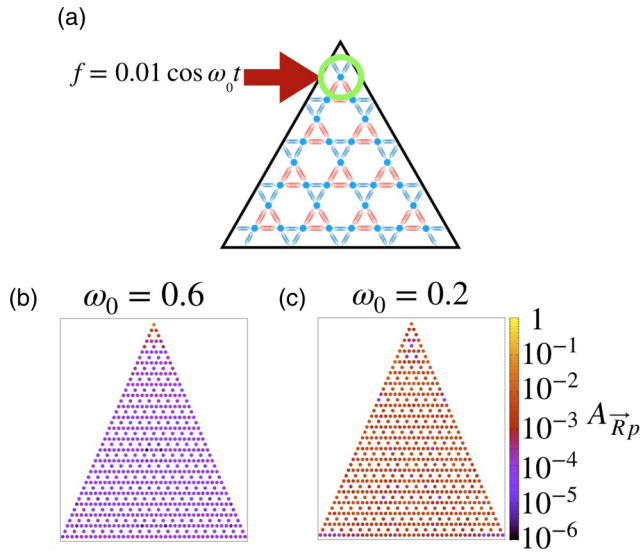

FIG. 6. (a) Schematic figure for the experimental setup for the forced vibration. The force $f(t)$ is added to the mass point of the top corner of the triangle (encircled by a green circle). (b) ω_0 is near a corner mode, and (c) ω_0 is away from a corner mode. In (b) and (c), the amplitudes $A_{\vec{R},p}$ at $t = 1000$ are plotted.

In the above we have focused on the case where η_a is small ($\eta_a = 0.1$). We can also observe the bulk-corner correspondence for $\eta_a = 0.9$, where the in-gap states are between the third and the fourth bands (see Appendix A). We also note that the corner states are also found in a parallelogram arrangement [14,15], which can also be understood in the same adiabatic connection argument (see Appendix D).

V. FORCED VIBRATION

In this section, we point out that corner states emerging from our spring-mass model can be experimentally observed by analyzing a forced vibration. The forced vibration is caused by an external force $f(t)$. The equation of motion with an external force is

$$\ddot{\vec{x}} + D\vec{x} = \vec{f}(t), \tag{25}$$

where $(f)_{\vec{R},p,\mu}(t) = f^{\mu}_{\vec{R},p}(t)$ is an external force which is added to the mass at $\vec{R} + \vec{r}_p$ along the μ direction.

Consider the case where the external force is given by $f^{\mu}_{\vec{R},p}(t) = F^{\mu}_{\vec{R},p} \cos(\omega_0 t)$; that is, it oscillates in time with the frequency ω_0. We further set $F^{\mu}_{\vec{R},p}$ such that it has amplitudes only at the top corner [Fig. 6(a)]. Then, as a particular solution of the equation of motion of Eq. (25), ξ'_i, which governs the behaviors of the long time scale, we get

$$\xi'_i = \begin{cases} \frac{\sum_j U_{ij} F_j}{\omega_i^2 - \omega_0^2} \cos \omega_0 t & \text{for} \quad \omega_i \neq \omega_0, \\ \frac{\sum_j U_{ij} F_j}{2\omega_0} t \sin \omega_0 t & \text{for} \quad \omega_i = \omega_0, \end{cases} \tag{26}$$

where U is a matrix obtained by aligning the eigenvectors of the equation of motion in the absence of $f(t)$ [i.e., Eq. (8)], i specifies the eigenmode, j is the abbreviation of the position of the mass point $\vec{R} + \vec{r}_p$ and the direction of the motion μ, and ω_i is the eigenfrequency of the ith mode. From Eq. (26), we see the resonance occurs at $\omega_i = \omega_0$. This indicates that for ω_0 close to the eigenfrequency of the corner state, one obtains the large vibration amplitude only at the corner; in contrast, when it is close to the eigenfrequency of the bulk state, the vibration spreads over the bulk. Thus, by looking at the time evolution of the forced vibration upon changing ω_0, one can determine whether the corner states exist or not.

To demonstrate this, we numerically solve the equation of motion using the Euler method on a triangle arrangement. In the Euler method, the time revolution is described as

$$\begin{pmatrix} \vec{x}(t + \Delta t) \\ \dot{\vec{x}}(t + \Delta t) \end{pmatrix} = \left\{ \begin{pmatrix} \hat{0} & \hat{1} \\ -D & \hat{0} \end{pmatrix} \begin{pmatrix} \vec{x}(t) \\ \dot{\vec{x}}(t) \end{pmatrix} + \begin{pmatrix} \vec{0} \\ \vec{f}(t) \end{pmatrix} \right\} \Delta t + \begin{pmatrix} \vec{x}(t) \\ \dot{\vec{x}}(t) \end{pmatrix}, \tag{27}$$

where Δt is a small time step. D is given in Eq. (25). For the numerical simulations, we set $\eta_a = 0.9$, $t_a/t_b = 0.1$, and $\Delta t = 0.0001$. It is worth noting that η is close to 1 for realistic springs. The initial state is set as $x^{\mu}_{\vec{R},p}(0) = 0$ and $\dot{x}^{\mu}_{\vec{R},p}(0) = 0$; that is, the system is in equilibrium. The external force in the x direction is added to the mass point at the top of the corner; we could not observe the qualitative difference when the external force is in the y direction. After running a simulation to $t = t_{\max} = 1000$, we observe the amplitudes of vibration,

$$A_{\vec{R},p} = \sqrt{\left[x^x_{\vec{R},p}(t_{\max})\right]^2 + \left[x^y_{\vec{R},p}(t_{\max})\right]^2}. \tag{28}$$

The results are shown in Figs. 6(b) and 6(c). As expected, when ω_0 is near the frequency of the corner state [57], the large vibration is seen only near the corner, while the vibration propagates in the bulk when ω_0 is near the frequency of the bulk state.

The above results suggest that the corner state induced by the topological properties in the bulk can be experimentally observed; the resonance frequency corresponds to the frequency of corner states.

VI. SUMMARY

In summary, we have shown that the higher-order topological phase is realized in the spring-mass model on a breathing kagome lattice. We have introduced the $\mathbb{Z}_3$ Berry phase in the Brillouin zone and found that our bulk topological invariant characterizes the topologically nontrivial phase. Remarkably, we have found the topologically nontrivial phase with $\gamma = \frac{2\pi}{3}$, in addition to the phase with $\gamma = \frac{4\pi}{3}$ that corresponds to the two copies of the topological phase in the tight-binding model. This is due to the coupling between longitudinal and transverse modes inherent in the spring-mass model. We have also found that the characteristic corner states appear under the fixed boundary condition in both the triangle and parallelogram arrangements. In addition, we have proposed that the corner states can be detected experimentally through a forced vibration. By the numerical simulation, we have found that the corner-selective vibration is observed when the external frequency is close to that of the corner modes.

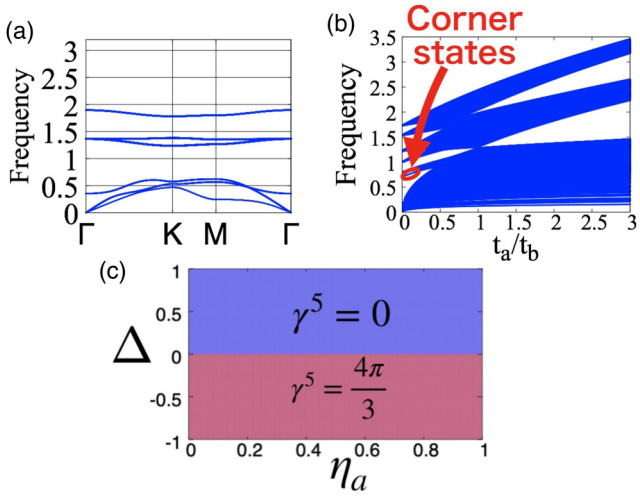

FIG. 7. (a) The bands structure for $\eta_a = 0.9$, $t_a/t_b = 0.1$. (b) The energy spectrum for $\eta_a = 0.9$. The corner modes are between the third and fourth bands. (c) The $\mathbb{Z}_3$ Berry phase for the lowest fifth bands.

ACKNOWLEDGMENTS

This work is partly supported by JSPS KAKENHI Grants No. JP16K13845, No. JP17H06138, No. JP18H05842, No. JP19J12315, and No. JP19K21032. Part of the numerical calculations was performed on the supercomputer at ISSP at the University of Tokyo.

APPENDIX A: $\mathbb{Z}_3$ BERRY PHASE FOR THE LOWEST FIVE BANDS

In this appendix, we show the result for γ^5, i.e., the Berry phase for the lowest five bands. The reason for calculating γ^5 is that there exist corner states that appear between the third and fourth bands for $\eta_a \sim 1$, contrary to the case of $\eta_a \sim 0$. To be concrete, we show the bulk band structure and the energy spectra in a triangle arrangement at $\eta_a = 0.9$ in Figs. 7(a) and 7(b), respectively, and the $\mathbb{Z}_3$ Berry phase for the lowest five bands.

We find that the band gap exists between the third and fourth bands and between the fifth and sixth bands, in contrast to the case of $\eta_a \sim 0$. Correspondingly, the corner states appear for a certain region for $t_a < t_b$, while there are no corner states for $t_a > t_b$, which is again inferred from the adiabatic connection argument.

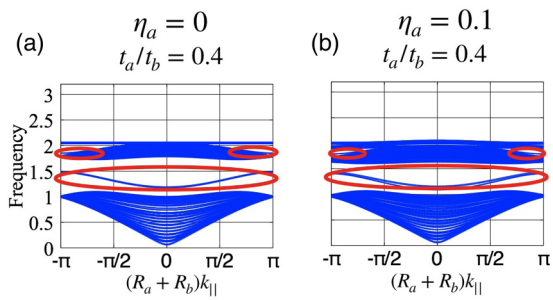

FIG. 8. The dispersion relations in the cylinder for (a) $\eta_a = 0$, $t_a/t_b = 0.4$ and (b) $\eta_a = 0.1$, $t_a/t_b = 0.4$. There exist edge modes between the bulk continua (encircled by red ellipses).

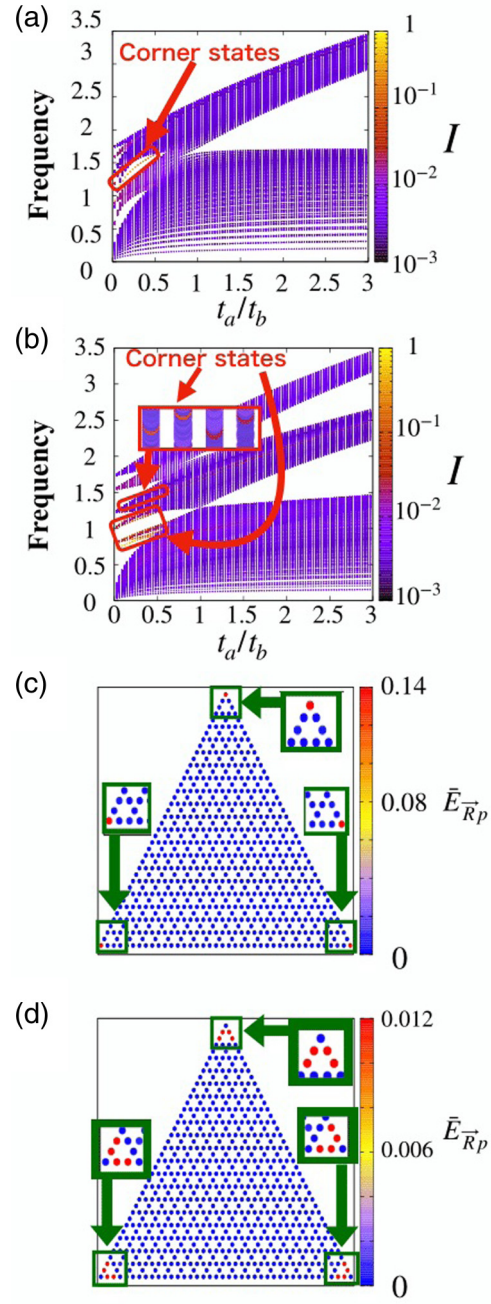

FIG. 9. (a) and (b) Color map of IPR in the figure of eigenfrequencies. (a) and (b) show the data for $\eta_a = 0.1$ and 0.9, respectively. Kinetic-energy distribution in the real space of the corner states for (c) $t_a/t_b = 0.2$, $\eta_a = 0.9$, $\omega = 1.3954$ and (d) $t_a/t_b = 0.2$, $\eta_a = 0.9$, $\omega = 0.854085$.

We plot γ^5 in Fig. 7(c), showing that $\mathbb{Z}_3$ is independent of η_a and the phase translation occurs at $\Delta = 0$, i.e., $t_a = t_b$. Similar to γ^2 discussed in Sec. III, $\gamma^5 = \frac{4\pi}{3}$ indicates that the system is adiabatically connected to the decoupled triangles with blue springs [Fig. 4(b)], while $\gamma^5 = 0$ indicates that the system is adiabatically connected to the decoupled triangles with red springs [Fig. 4(c)].

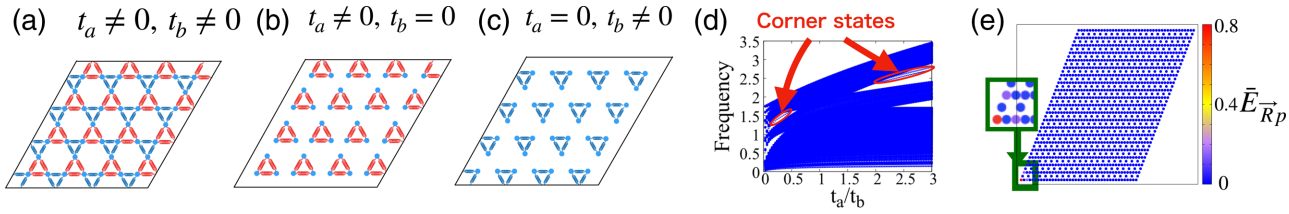

FIG. 10. Schematic figures for the spring-mass model in a parallelogram arrangement with (a) $t_a \neq 0,\ t_b \neq 0$, (b) $t_a \neq 0,\ t_b = 0$, and (c) $t_a = 0,\ t_b \neq 0$. Black lines represent walls. (d) Eigenfrequencies as a function of t_a/t_b for $\eta_a = 0.1$ with a parallelogram arrangement. (e) Kinetic-energy distribution in the real space of the corner states for $t_a/t_b = 0.4$. The corner mode for $\gamma = 0$ arises from the fact that we have cut the unit cells which make the bulk-edge correspondence ubiquitous.

APPENDIX B: THE CYLINDER OF THE SPRING-MASS MODEL

In this appendix, we show the dispersion relations on the cylinder geometry, focusing on the features of the edge states. Here, we set the number of red springs in the axial direction as 20, and we write the momentum in the azimuth direction $k_{||}$.

The results are shown in Fig. 8. We see that there exist edge modes between bulk continua, whose real-space distributions are localized at the edge. Importantly, the edge mode is not energetically connected to the bulk continuum, meaning that the lower-dimensional boundary states, i.e., the corner states, are allowed to exist between the edge modes and the bulk modes.

APPENDIX C: INVERSE PARTICIPATION RATIO

In this section, we show the numerical result of the IPR to specify the corner states buried in the bulk or edge continuum. In the literature, the IPR has been used to study Anderson localization in disordered systems [58,59], and it was recently used to specify the corner states in the HOTI [60]. The IPR in the spring-mass model is defined as

$$I = \sum_{\vec{R}} \sum_{p} \left\{ \sum_{\mu} \left(\xi^{\mu}_{\vec{R},p} \right)^2 \right\}^2, \tag{C1}$$

where $\vec{\xi}$ stands for the normalized eigenvector. For the extended states, the relation $\sum_{\mu} (\xi^{\mu}_{\vec{R},p})^2 \simeq 1/N$ holds, which results in $I \simeq 1/N$. Therefore, the IPR for the extended states vanishes in the large-system-size limit. In contrast, for the corner states, the relation $\sum_{\mu} (\xi^{\mu}_{\vec{R},p})^2 \simeq \delta_{\vec{R},\vec{R}_c} \delta_{p,p_c}$ holds, which results in $I \simeq 1$. Here, $(\vec{R}_c,\ p_c)$ denotes the corner site.

The numerical result is shown in Fig. 9. We see that the corner modes in the bulk or edge continuum are specified by the large IPR [Fig. 9(c)].

Additionally, we find the "cornerlike" modes, where the eigenvector has large amplitudes not right at the corners but at the sites near the corners [Fig. 9(d)]. Such modes appear for large η ($\eta = 0.9$ in this case); thus, they are characteristic of the spring-mass model.

APPENDIX D: PARALLELOGRAM ARRANGEMENT UNDER THE FIXED BOUNDARY CONDITION

In this appendix, we show the results for a parallelogram arrangement [Fig. 10(a)]. Specifically, we show the corner modes in the parallelogram arrangement and their bulk-corner correspondence.

In this arrangement, we write the number of small triangles along the edge as L. Then, the number of total masses is $3L^2 + 4L + 1$.

In Fig. 10(d), we plot the energy spectra as a function of t_a/t_b for $L = 20$ and $\eta_a = 0.1$. As expected, we see the in-gap states for both $t_a < t_b$ and $t_a > t_b$. Looking at the spatial distribution of the kinetic energy of the in-gap states for $t_a < t_b$, we find that it is localized at the left-bottom corner [Fig. 10(e)].

The bulk-corner correspondence in the system is explained as follows. As we saw in Sec. III, $\gamma^2 = 4\pi/3$ indicates that the band structure is adiabatically connected to that for $t_a = 0$ [Fig. 4(b)]; similarly, $\gamma^2 = 0$ indicates that the band structure is adiabatically connected to that for $t_b = 0$ [Fig. 4(c)]. This means that the former case has the corner state at the top right corner [Fig. 10(b)] and the latter case has the corner state at the bottom left corner [Fig. 10(c)].

[1] M. Z. Hasan and C. L. Kane, Rev. Mod. Phys. **82**, 3045 (2010).
[2] X.-L. Qi and S.-C. Zhang, Rev. Mod. Phys. **83**, 1057 (2011).
[3] F. D. M. Haldane, Phys. Rev. Lett. **61**, 2015 (1988).
[4] C. L. Kane and E. J. Mele, Phys. Rev. Lett. **95**, 226801 (2005).
[5] X.-L. Qi, T. L. Hughes, and S.-C. Zhang, Phys. Rev. B **78**, 195424 (2008).
[6] A. M. Essin, J. E. Moore, and D. Vanderbilt, Phys. Rev. Lett. **102**, 146805 (2009).
[7] Y. Hatsugai, Phys. Rev. Lett. **71**, 3697 (1993).
[8] Y. Hatsugai, Phys. Rev. B **48**, 11851 (1993).
[9] S. Hayashi, Commun. Math. Phys. **364**, 343 (2018).
[10] W. A. Benalcazar, B. A. Bernevig, and T. L. Hughes, Science **357**, 61 (2017).
[11] W. A. Benalcazar, B. A. Bernevig, and T. L. Hughes, Phys. Rev. B **96**, 245115 (2017).
[12] M. Ezawa, Phys. Rev. Lett. **120**, 026801 (2018).

[13] F. Schindler, A. M. Cook, M. G. Vergniory, Z. Wang, S. S. P. Parkin, B. A. Bernevig, and T. Neupert, Sci. Adv. **4**, eaat0346 (2018).

[14] F. K. Kunst, G. van Miert, and E. J. Bergholtz, Phys. Rev. B **97**, 241405(R) (2018).

[15] Y. Xu, R. Xue, and S. Wan, arXiv:1711.09202.

[16] D. Călugăru, V. Juričić, and B. Roy, Phys. Rev. B **99**, 041301(R) (2019).

[17] B. Kang, K. Shiozaki, and G. Y. Cho, Phys. Rev. B **100**, 245134 (2019).

[18] T. Fukui and Y. Hatsugai, Phys. Rev. B **98**, 035147 (2018).

[19] Y. Hatsugai and I. Maruyama, Europhys. Lett. **95**, 20003 (2011).

[20] K. Kudo, T. Yoshida, and Y. Hatsugai, Phys. Rev. Lett. **123**, 196402 (2019).

[21] H. Araki, T. Mizoguchi, and Y. Hatsugai, Phys. Rev. Res. **2**, 012009 (2020).

[22] M. Ezawa, Phys. Rev. B **98**, 045125 (2018).

[23] F. Schindler, Z. Wang, M. G. Vergniory, A. M. Cook, A. Murani, S. Sengupta, A. Y. Kasumov, R. Deblock, S. Jeon, I. Drozdov, H. Bouchiat, S. Guéron, A. Yazdani, B. A. Bernevig, and T. Neupert, Nat. Phys. **14**, 918 (2018).

[24] X.-L. Sheng, C. Chen, H. Liu, Z. Chen, Z.-M. Yu, Y. X. Zhao, and S. A. Yang, Phys. Rev. Lett. **123**, 256402 (2019).

[25] E. Lee, R. Kim, J. Ahn, and B.-J. Yang, npj Quantum Mater. **5**, 1 (2020).

[26] J. M. Lee, C. Geng, J. W. Park, M. Oshikawa, S.-S. Lee, H. W. Yeom, and G. Y. Cho, arXiv:1907.00012.

[27] T. Mizoguchi, M. Maruyama, S. Okada, and Y. Hatsugai, Phys. Rev. Mater. **3**, 114201 (2019).

[28] M. Serra-Garcia, V. Peri, R. Süsstrunk, O. R. Bilal, T. Larsen, L. G. Villanueva, and S. D. Huber, Nature (London) **555**, 342 (2018).

[29] J. Attig, K. Roychowdhury, M. J. Lawler, and S. Trebst, Phys. Rev. Res. **1**, 032047(R) (2019).

[30] A. El Hassan, F. K. Kunst, A. Moritz, G. Andler, E. J. Bergholtz, and M. Bourennane, Nat. Photonics **13**, 697 (2019).

[31] Y. Ota, F. Liu, R. Katsumi, K. Watanabe, K. Wakabayashi, Y. Arakawa, and S. Iwamoto, Optica **6**, 786 (2019).

[32] X. Ni, M. A. Gorlach, A. Alu, and A. B. Khanikaev, N. J. Phys. **19**, 055002 (2017).

[33] H. Xue, Y. Yang, F. Gao, Y. Chong, and B. Zhang, Nat. Mater. **18**, 108 (2019).

[34] X. Ni, M. Weiner, A. Alù, and A. B. Khanikaev, Nat. Mater. **18**, 113 (2019).

[35] S. Imhof, C. Berger, F. Bayer, J. Brehm, L. W. Molenkamp, T. Kiessling, F. Schindler, C. H. Lee, M. Greiter, T. Neupert, and R. Thomale, Nat. Phys. **14**, 925 (2018).

[36] M. Ezawa, Phys. Rev. B **98**, 201402(R) (2018).

[37] S. N. Kempkes, M. R. Slot, J. J. van den Broeke, P. Capiod, W. A. Benalcazar, D. Vanmaekelbergh, D. Bercioux, I. Swart, and C. Morais Smith, Nat. Mater. **18**, 1292 (2019).

[38] C. Kane and T. Lubensky, Nat. Phys. **10**, 39 (2014).

[39] Y.-T. Wang, P.-G. Luan, and S. Zhang, N. J. Phys. **17**, 073031 (2015).

[40] T. Kariyado and Y. Hatsugai, Sci. Rep. **5**, 18107 (2015).

[41] Y. Takahashi, T. Kariyado, and Y. Hatsugai, N. J. Phys. **19**, 035003 (2017).

[42] Y. Takahashi, T. Kariyado, and Y. Hatsugai, Phys. Rev. B **99**, 024102 (2019).

[43] T. Yoshida and Y. Hatsugai, Phys. Rev. B **100**, 054109 (2019).

[44] For $\eta_\alpha = 0$, we consider the situation where $l_\alpha \to 0$ while keeping R_α unity .

[45] Y. Hatsugai, J. Phys. Soc. Jpn. **75**, 123601 (2006).

[46] Y. Hatsugai, J. Phys.: Condens. Matter **19**, 145209 (2007).

[47] T. Hirano, H. Katsura, and Y. Hatsugai, Phys. Rev. B **77**, 094431 (2008).

[48] Y. Hatsugai, N. J. Phys. **12**, 065004 (2010).

[49] Y. Motoyama and S. Todo, Phys. Rev. E **87**, 021301(R) (2013).

[50] N. Chepiga, I. Affleck, and F. Mila, Phys. Rev. B **94**, 205112 (2016).

[51] T. Kariyado, T. Morimoto, and Y. Hatsugai, Phys. Rev. Lett. **120**, 247202 (2018).

[52] Y. Motoyama and S. Todo, Phys. Rev. B **98**, 195127 (2018).

[53] T. Kawarabayashi, K. Ishii, and Y. Hatsugai, J. Phys. Soc. Jpn. **88**, 045001 (2019).

[54] T. Mizoguchi, H. Araki, and Y. Hatsugai, J. Phys. Soc. Jpn. **88**, 104703 (2019).

[55] W. P. Su, J. R. Schrieffer, and A. J. Heeger, Phys. Rev. Lett. **42**, 1698 (1979).

[56] T. Fukui, Y. Hatsugai, and H. Suzuki, J. Phys. Soc. Jpn. **74**, 1674 (2005).

[57] Note that, if ω_0 is exactly at the frequency of the corner state, the resonance occurs, which results in the breakdown of the approximation of the small displacement .

[58] S. Yoshino and M. Okazaki, J. Phys. Soc. Jpn. **43**, 415 (1977).

[59] M. Janssen, Phys. Rep. **295**, 1 (1998).

[60] H. Araki, T. Mizoguchi, and Y. Hatsugai, Phys. Rev. B **99**, 085406 (2019).